Journal of Zhejiang University-SCIENCE A (Applied Physics & Engineering) in press
www.jzus.zju.edu.cn; www.springer.com/journal/11582
E-mail: jzus_a@zju.edu.cn

Research Article

https://doi.org/10.1631/jzus.A2400018

Effects of dry–wet cycling on the mechanical properties and microscopic characteristics of fine breccia soil from karst areas

Xin LI[1,2,3], Hanqing CHEN[1,2,3]✉, Dong SU[1,2,3], Xiangsheng CHEN[1,2,3], Xiang SHEN[1,2,3]

[1]*College of Civil and Transportation Engineering, Underground Polis Academy, Shenzhen University, Shenzhen 518060, China*
[2]*Key Laboratory of Coastal Urban Resilient Infrastructures, Shenzhen University, Ministry of Education, Shenzhen 518060, China*
[3]*Shenzhen Key Laboratory of Green, Efficient, and Intelligent Construction of Underground Metro Station, Shenzhen 518060, China*

Abstract: The quality of roadbed engineering is directly related to the fill soil structure, which, in turn, is determined by the physical and chemical environment of a given area. The karst water environment, with frequent rainfall events, promotes the dissolution of soluble rocks and transportation of underground substances, which alters the soil structure and performance. Therefore, we aimed to analyze the properties of underground soil from heavily developed karst areas. Fine breccia soil from karst regions was tested to assess its macroscopic mechanical properties and microstructural features at various initial water contents and compaction levels. Samples were subjected to simulated rainfall conditions, undergoing dry–wet cycling, followed by triaxial shear testing and electron microscopy examinations. From the data obtained, a micro-to-macro correlation and normalization model were developed. The findings suggest that the resistance of fine angular breccia soil to degradation upon to dry–wet cycling can be enhanced by high-pressure compaction and maintaining a moisture content close to the optimal level. Increasing the degree of compaction improves the particle size distribution and skeleton density of the soil. This is advantageous for minimizing soil particle erosion, thereby ensuring the robust performance of roadbeds in karst areas with frequent rainfall events.

Key words: Karst area; Micro–macro properties; Roadbed performance; Dry–wet cycles

1 Introduction

The full and reasonable utilization of land resources to achieve environmentally friendly construction is one of the main goals of railway engineering. In particular, roadbed construction follows the basic principle of locally sourced materials, excavation, and filling. The quality of roadbed engineering is directly related to the fill soil, which, in turn, is determined by the physical and chemical environment of a given area and is, therefore, region-specific (Xu *et al.*, 2019; Ibrahim *et al.*, 2022; Raja *et al.*, 2022; Sun *et al.*, 2021; Xiao, 2007). Karst areas feature a unique ecological setting with a wide distribution of underground soluble rocks and a complex correlation between surface and groundwater environments. The karst water environment promotes the dissolution of soluble rocks, the transportation and deposition of underground substances, and other processes that alter the soil structure and performance (Xin *et al.*, 2021; Wang, 2014; Deng *et al.*, 2020; Smirnova and Gennadiev, 2011). Notably, this is the case even after filling and operation in karst areas. When the underground soil in karst areas is used for roadbed fill, the project remains in a rainfall-intensive karst environment. Given the long-term influence of repeated rainfall infiltration and underground karst water seepage-induced erosion on the performance of roadbed soil, the effect of dry–wet cycling on the mechanical and deformation characteristics of soil in karst areas is of high practical significance (Celauro *et al.*, 2017; Lu *et al.*, 2020; Mu *et al.*, 2016; Geng *et al.*, 2022). However, as macroscopic performance is closely related to microstructural characteristics, the interpretation of macroscopic changes from a microscopic perspective can help us better understand the characteristics of roadbed soil structures and the mechanical properties of roadbeds

✉ Hanqing CHEN, hanqingchen@suz.edu.cn
Hanqing CHEN, https://orcid.org/0000-0002-2115-3538

Received Jan. 12, 2024; Revision accepted Aug. 12, 2024;
Crosschecked

© Zhejiang University Press 2024

Uncorrected

in karst areas (Luo *et al.*, 2022; Mingjing, 2019).

The durability- and strength-related characteristics of roadbed fill materials must be evaluated to assess their fitness for use. The inherent characteristics of soils formed under different conditions and their long-term performance in complex environments are important factors affecting roadbed service quality (Xu *et al.*, 2019; Khalid *et al.*, 2022; Song *et al.*, 2015; Feng and Lei, 2022; Zhou, 2012; Han *et al.*, 2016). Consequently, research on the characteristics and long-term performance of karst soil exposed to such environments is required to improve its performance as roadbed fill.

The performance of roadbed fill and the durability of filled roadbeds in certain areas have been investigated extensively. Scholars have conducted in-depth analyses on different types of roadbed fill, including performance soils, blended soils, soils from special regions, and recycled fine-particle waste materials, from the perspectives of micro-mechanisms and macro-mechanical properties. They have studied how the mechanical properties and applicability of various soils are affected by their chemical and physical particle compositions, and proposed corresponding mechanical models (Chen *et al.*, 2019; Z. Li *et al.*, 2022; Que *et al.*, 2022; Drobinina *et al.*, 2020).

Numerous researchers have examined the evolution of the mechanical properties of soil under dry–wet cycling. Chao *et al.* (2023) studied the consolidated undrained triaxial shear characteristics of soil under the combined action of dry–wet cycling and vertical confining pressure, showing that the first dry–wet cycle had the most significant impact on soil matric suction, while the vertical confining pressure could limit the impact of cycling on the hydraulic properties of the soil. Other researchers have studied the shear strength, compressive properties, water–soil properties, participating strength, and tensile properties of sandy kaolin, coarse-grained soil, Guangxi clay, coal-bearing soil, and red clay under different dry–wet cycling conditions. The initial dry–wet cycle typically has the greatest impact on soil properties (albeit with a certain lag), and corresponding damage constitutive equations have been established (Goh *et al.*, 2014; S. Li *et al.*, 2022; Wen *et al.*, 2021; Zeng *et al.*, 2022; Huang and Zheng, 2021). Fang *et al.* (2021) studied the effects of dry–wet cycling on the mechanical properties of expansive soil and found that cycling reduced cohesion and the internal friction angle. The suction friction angle after dry–wet cycling varied under suction conditions of ≤200 kPa and tended to stabilize after three cycles. Li *et al.* (2017) studied the effect of dry–wet cycling on highway roadbed silty clay and proposed a mechanism for the resulting damage. Yu *et al.* (2019) studied the influences of dry–wet cycling on the shear strength and slope stability of granite residual soil and derived a corresponding safety factor for slope stability. They found that the shear strength stabilized after three to five cycles. Lu *et al.* (2020) combined the results of laboratory experiments and numerical simulations to model the long-term deformation of a roadbed exposed to traffic loads and dry–wet cycling, dividing this deformation into three stages and establishing corresponding models. The results showed that the amplitude of dry–wet cycling had a greater impact on roadbed deformation than confining pressure variation, suggesting that in practice, the range of variation in roadbed moisture content must be carefully controlled.

Considerable efforts have been directed at explaining macroscopic mechanical phenomena from a microstructural perspective (Kong *et al.*, 2022). The microstructural parameters are correlated with macroscopic indicators. By using techniques such as triaxial testing, penetration testing, nuclear magnetic resonance, and scanning electron microscopy (SEM), researchers have attempted to explain the mechanisms behind this relationship (Hu *et al.*, 2021; Li and Liu, 2020; Wang *et al.*, 2022; Yong *et al.*, 2020; Lin and Cerato, 2015; Yuan *et al.*, 2021).

Although some studies have dealt with special roadbed fill, soil property evolution in response to dry–wet cycling, and micro–macro soil mechanics, in-depth research on the mechanical properties and roadbed fill performance of *in situ* soil in karst areas is lacking. In addition, considering the rainfall-intensive nature of karst areas, research on the damage mechanisms and microscopic characteristics of soil subjected to dry–wet cycling in such areas is scarce. Consequently, further research is needed to reveal the relevant mechanisms and provide corresponding guidance and suggestions.

To address the aforedescribed gap, this study focused on the physical and mechanical properties, microstructural characteristics, micro–macro charac-

Uncorrected

teristic correlation, and damage model of *in situ* roadbed fill in karst areas under long-term dry–wet cycling. The object of the analysis was underground soil from heavily developed karst areas. Triaxial shear testing of soil samples with different moisture contents subjected to zero, two, four, and six dry–wet cycles was conducted, with each cycle involving 12-h drying and 12-h vacuum saturation. Different experiments were conducted to obtain the failure strengths, elastic moduli, shear parameters, particle size distributions, and void particle ratios of soil samples under different conditions. Finally, we propose a damage model for underground soil in karst areas subjected to dry–wet cycling; to our knowledge, this is one of the only works to do so. The results of unconsolidated and undrained triaxial tests were used to analyze the macroscopic mechanical characteristics of soil in karst areas. SEM imaging and graphical feature extraction and quantification were conducted using Image Pro Plus.V6 (IPP.V6) to examine the microscopic characteristics of karst soil under different conditions and provide relevant suggestions for engineering practice.

2 Methodology

2.1 Materials

The soil used in this study, a natural fine breccia soil found in karst areas, was collected in Xinyu City (Jiangxi Province, China) and used as a fill for nearby heavy-railway subgrade projects. The soil collection area receives a large amount of rainfall and can be classified as a densely developed karst area featuring soluble rocks and underground rivers and characterized by frequent soil cave collapses. Soil was excavated from a depth of 1.5 m in developed karst areas and transported to the laboratory. The particle size distribution was determined using a screening method, and the soil was characterized in terms of its liquid and plastic limits, compaction, and chemical composition. The soil sampling and treatment processes are illustrated in Fig. 1, and the particle size distribution is provided in Table 1. Just 0.39% of the soil passed through the 0.075 mm sieve, and the content of particles with sizes of 2–5 mm (gravel) exceeded 50%. The non-uniformity coefficient exceeded 5, and the curvature coefficient ranged from 1 to 3. Thus, the collected soil was identified as well-graded fine breccia soil with a fine particle composition of silty clay. The soil's bulk density (1.69 g/cm^3) was measured by drying and weighing, with a specific gravity and porosity of 2.52 g/cm^3 and 32%, respectively. After drying, crushing, and passing through a 0.5-mm sieve, the fine-grained components in the 1.5-m layer of soil were determined using a combined liquid–plastic limit tester, with the plastic and liquid limits being 15.1% and 29.3%, respectively.

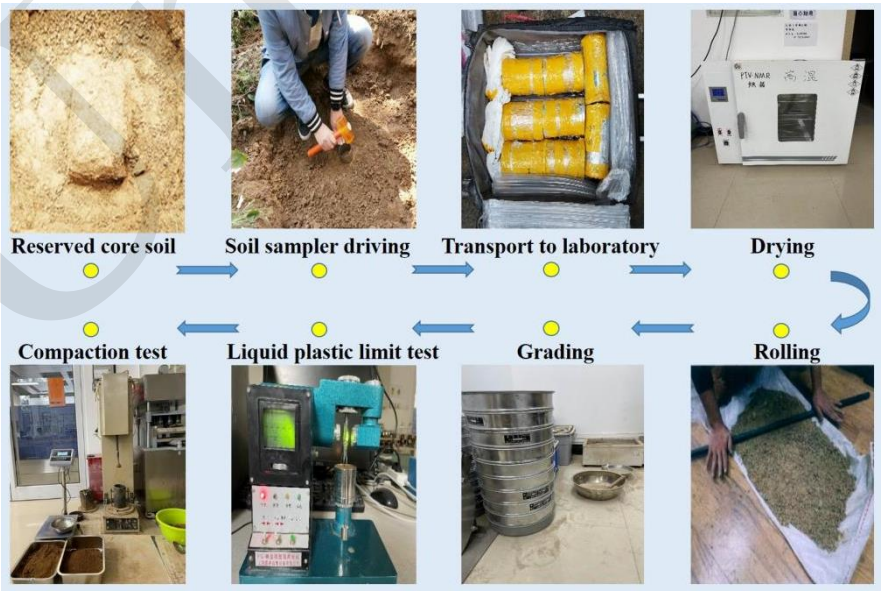

Fig. 1 Soil collection and basic property analysis

Table 1 Soil particle size distribution (% particles smaller than a certain size).

Particle size (mm)	10	5	2	1	0.5	0.25	0.1	0.075
Content (%)	99.78	73.9	30.98	15.79	7.6	3.84	0.82	0.39

We prepared five soil samples with moisture contents of ±2% and ±4%, taking the measured plastic limit of the soil as the median. Compaction tests were conducted on these samples to construct a compaction curve (Fig. 2). The optimal moisture content and maximum dry density of the 1.5-m-layer soil were determined to be 15.6% and 1.85 g/cm^3, respectively. The chemical composition was analyzed using X-ray fluorescence spectroscopy (Fig. 3).

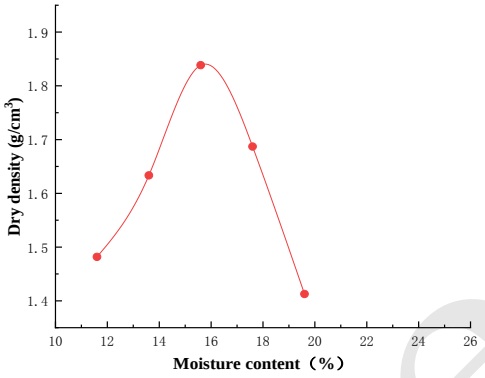

Fig. 2 Compaction curve

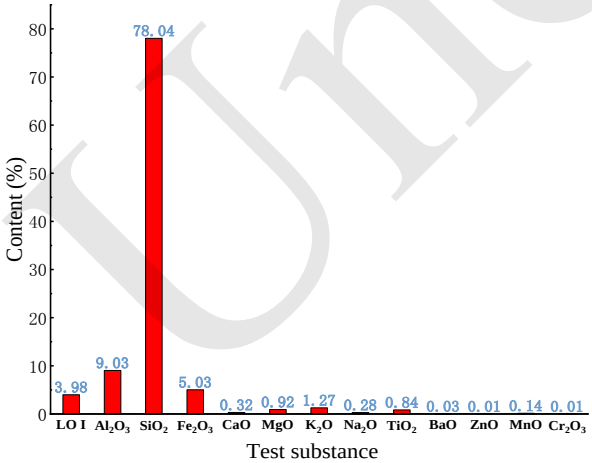

Fig. 3 Main chemical components of soil (LOI = loss on ignition)

2.2 Test methods

Dry–wet cycling has a long-term impact on the internal structure and mechanical properties of soil. Two basic variables, confining pressure and the number of dry–wet cycles, as well as two selective variables, initial moisture content and compaction degree, were used to conduct undrained and unconsolidated triaxial shear tests. A single-variable parallel comparison test method was employed based on on-site and roadbed engineering characteristics. Representative samples were selected for microstructural analysis by SEM imaging. Confining pressures of 150, 250, and 350 kPa were selected, considering the stress state of railway subgrade and the range of commonly used confining pressures. Prior research suggests that the internal structure and deformation characteristics of soil reach a stable state after approximately five dry–wet cycles (Liu, 2015). Tests were therefore conducted after zero, two, four, and six dry–wet cycles. Moisture content selection aimed to determine the optimal moisture content within 2% (±2%). The degree of compaction was based on the standard requirement that the degree of compaction of roadbed fill in China should equal or exceed 90%. Considering the requirements for increased compaction in heavy-duty areas, compaction values of 93%, 95%, and 97% were selected. The experimental design is illustrated in Fig. 4.

Triaxial testing was performed using an automated triaxial testing apparatus (TSZ-1). Soil collected indoors on site was crushed, dried, and passed through a 0.5-mm sieve. Water was added according to the initial moisture content requirements, and the samples were cured for 24 h. In accordance with the test specifications, each soil sample was placed and compacted in a cylindrical mold, producing a test specimen with dimensions of φ 39.1 mm × 80 mm.

For dry–wet cycling, the soil sample was placed in a three-petal mold saturator, exposed to vacuum, saturated in a saturation pot, and left to stand for 24 h to ensure sufficient saturation. The saturated sample was held at room temperature (approximately 25 ℃) for 24 h for natural air drying. The sample was placed in a closed box at night to simulate the higher evaporation rate in the daytime. The sample was taken out of the box in the morning and air-dried at room temperature to complete one dry–wet cycle. The above process was repeated for the desired number of cycles. The sample preparation and testing are illustrated in Fig. 5.

Uncorrected

For SEM analysis, the triaxial sample tested under the selected working conditions was broken apart and transferred to a small cube with a side length of 5 mm. The cubic test block was placed into an aluminum box and oven-dried for 48 h to ensure the complete evaporation of moisture from the internal pores of the soil. The sample surface was blow-dried and vacuum-sprayed with gold, then imaged using an E5200 SEM. IPP.V6 was used to adjust the color rendering of the target object based on imaging results. Color separation selection tools were used to select the target object, and data collectors and measurement tools were used to analyze the selected area and extract quantitative information. The related experimental and data extraction processes are illustrated in Fig. 6.

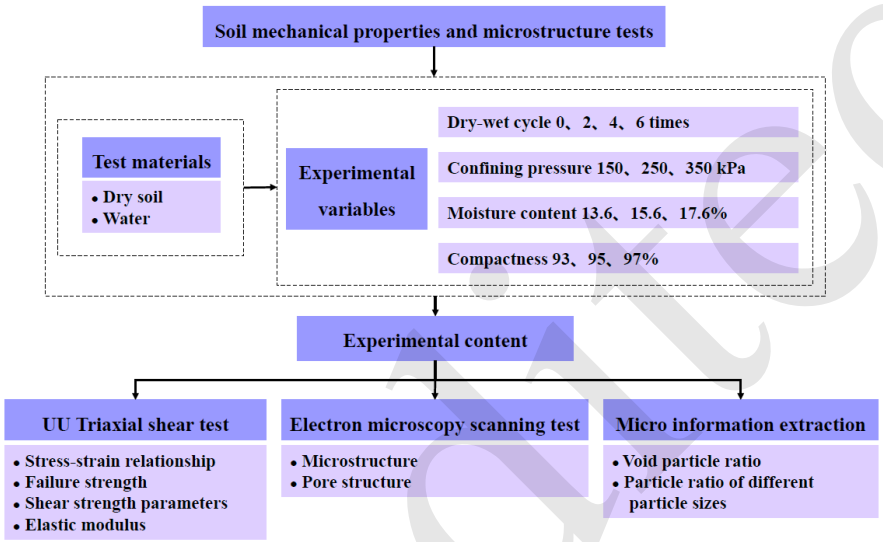

Fig. 4 Experimental design

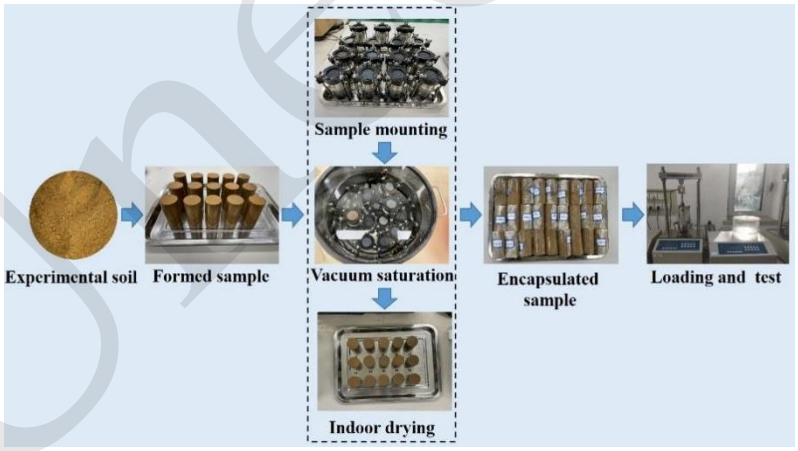

Fig. 5 Sample forming for triaxial shear test after dry–wet cycling

Uncorrected

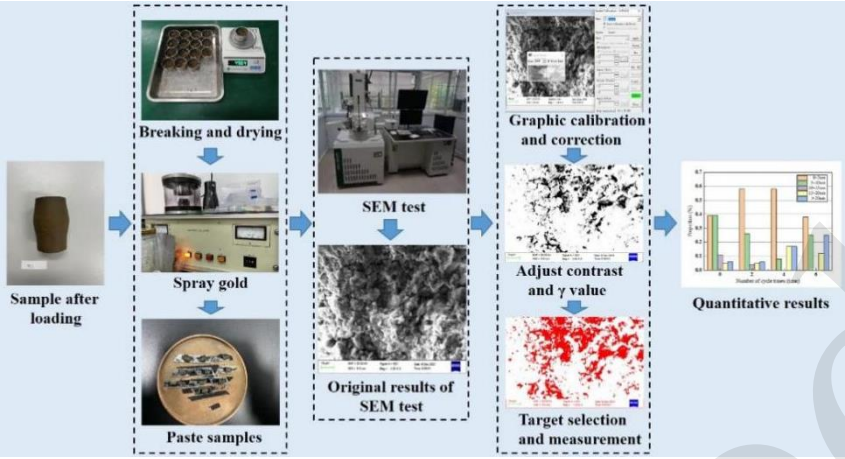

Fig. 6 Illustration of scanning electron microscopy imaging and related data extraction procedures

3 Results and discussion

3.1 Effects of dry–wet cycling on soil mechanical properties

3.1.1 Stress–strain relationship

Fig. 7 shows the deviatoric stress–strain curves obtained for different samples. At a constant compaction degree (Figs. 7a–7c) or initial moisture content (Figs. 7f–7i), the soil samples exhibited stress hardening, with the peak stress increasing with increasing confining pressure. For example, at confining pressures of 150, 250, and 350 kPa, the samples with an initial moisture content of 15.6% (Figs. 7f–7i) and zero dry–wet cycles exhibited peak stresses of 433.90 (+0%), 544.04 (+25%), and 798.15 (+47%) kPa, respectively. At a constant confining pressure (Figs. 7b, 7d, and 7e) or compaction degree (Figs. 7a–7c), the peak stress generally decreased with increasing dry–wet cycles.

At a constant confining pressure of 250 kPa (Figs. 7b, 7d, and 7e), the peak stress typically increased with increasing compaction degree. For example, the peak stresses of the samples with compaction degrees of 93%, 95%, and 97% were 439.9, 580.8, and 753.1 kPa, respectively, after two dry–wet cycles. At 97% compaction (Fig. 7e), samples with different numbers of dry–wet cycles exhibited similar trends, and the spacing between the curves decreased. In other words, increasing the compaction degree reduced the impact of dry–wet cycling on the soil performance degradation.

At a given compaction degree, the peak stress decreased as the initial moisture content increased (Figs. 7g, 7i, and 7j). For example, at zero dry–wet cycles and a confining pressure of 250 kPa, the peak stresses were 769.80 (−0%), 544.04 (−29%), and 326.32 (−40%) kPa for initial moisture contents of 13.6%, 15.6%, and 17.6%, respectively. In addition, at the optimal initial moisture content of 15.6% (Fig. 7f–7h), the spacing between the curves of the samples with different numbers of dry–wet cycles was smaller than that for samples with initial moisture contents of 13.6% or 17.6%, which suggests that the sample with the optimal initial moisture content was more resistant to cycling-induced degradation under the same conditions.

Unedited

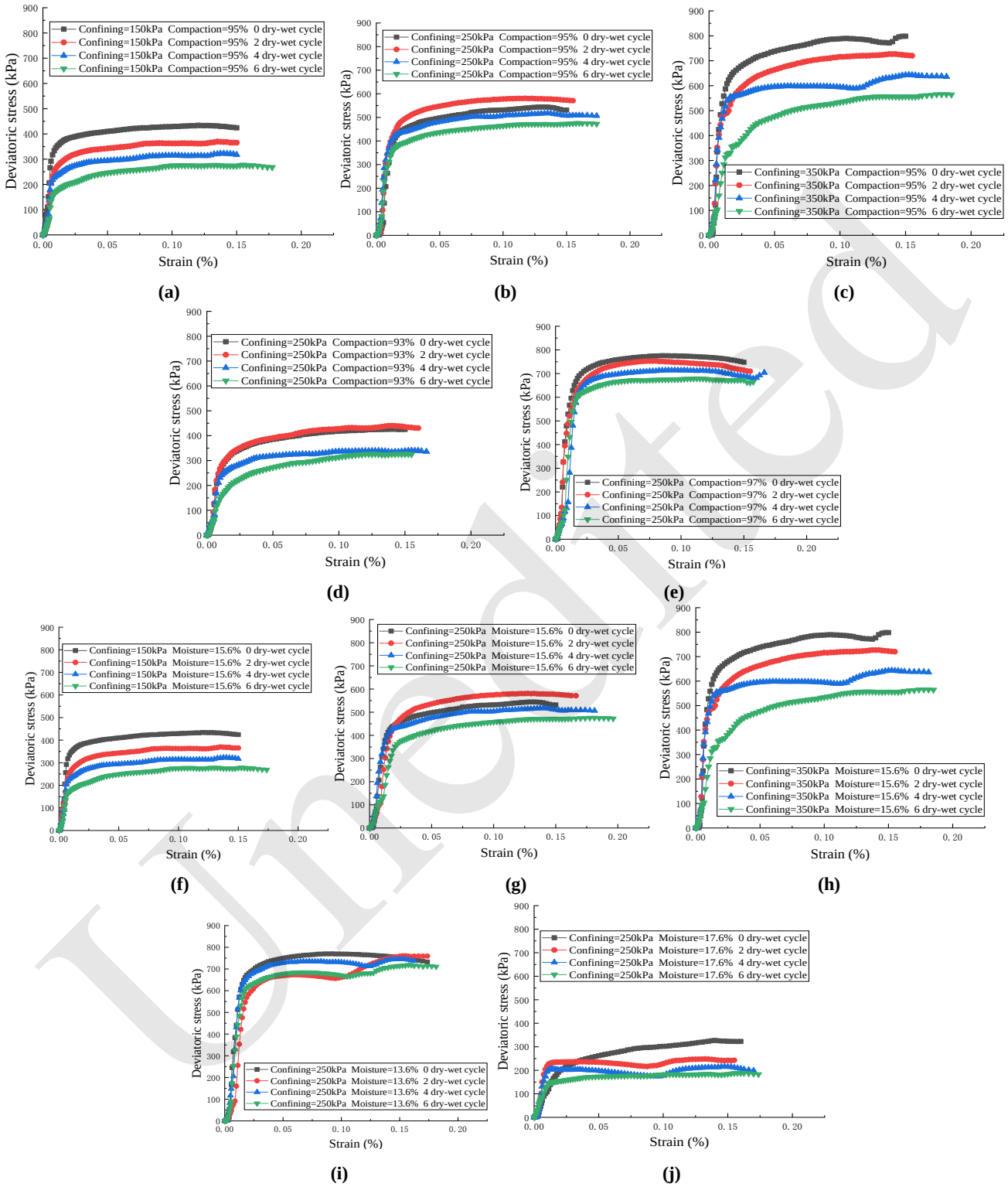

Fig. 7. Stress–strain curves during triaxial shear testing of different samples. Effects of (a)–(c) confining pressure (150, 250, and 350 kPa, respectively) at a constant compaction degree (95%); (d), (e) compaction degree (93% and 97%, respectively) at a constant confining pressure (250 kPa); (f)–(h) confining pressure (150, 250, and 350 kPa, respectively) at a constant initial moisture content (15.6%); and (i), (j) initial moisture content (13.6% and 17.6%, respectively) at a constant confining pressure (250 kPa). Each plot shows curves for samples after zero (gray), two (red), four (blue), and six (green) dry–wet cycles

Unedited

3.1.2 Failure strength

The failure strength of engineering soil that exhibits stress hardening behavior is typically considered to be equal to the deviatoric stress at a strain of 15%. As shown in Fig. 8a, at 15.6% initial moisture, the failure strength increased with increasing compaction degree, although the difference between the 95% and 97% samples was generally smaller than that between the 93% and 95% samples. At a constant confining pressure, the failure strength increased with increasing compaction degree (Fig. 8a) and decreased with increasing dry–wet cycling (Fig. 8b). The decrease with dry–wet cycling was relatively small at 97% compaction compared to that at 93% and 95% compaction, which indicates that a higher compaction degree provides better resistance to cycling-induced degradation.

Figs. 8c and 8d show that increasing the initial moisture content gradually decreased the failure strength at a constant compaction degree. Within six dry–wet cycles, the failure strength decreased and gradually stabilized at medium and low confining pressures but continued to increase at a high confining pressure. The failure strength at different initial moisture contents decreased and finally stabilized with increasing dry–wet cycles. Samples with initial moisture contents of 13.6%, 15.6%, and 17.6% and dry–wet cycles of zero/six had failure strengths of 769.80/718.65, 544.03/475.48, and 326.32/187.88 kPa, respectively. Thus, after six dry–wet cycles, the failure strength decreased by 6.64%, 12.60%, and 42.42%, respectively; that is, the magnitude of this decrease increased with increasing moisture content.

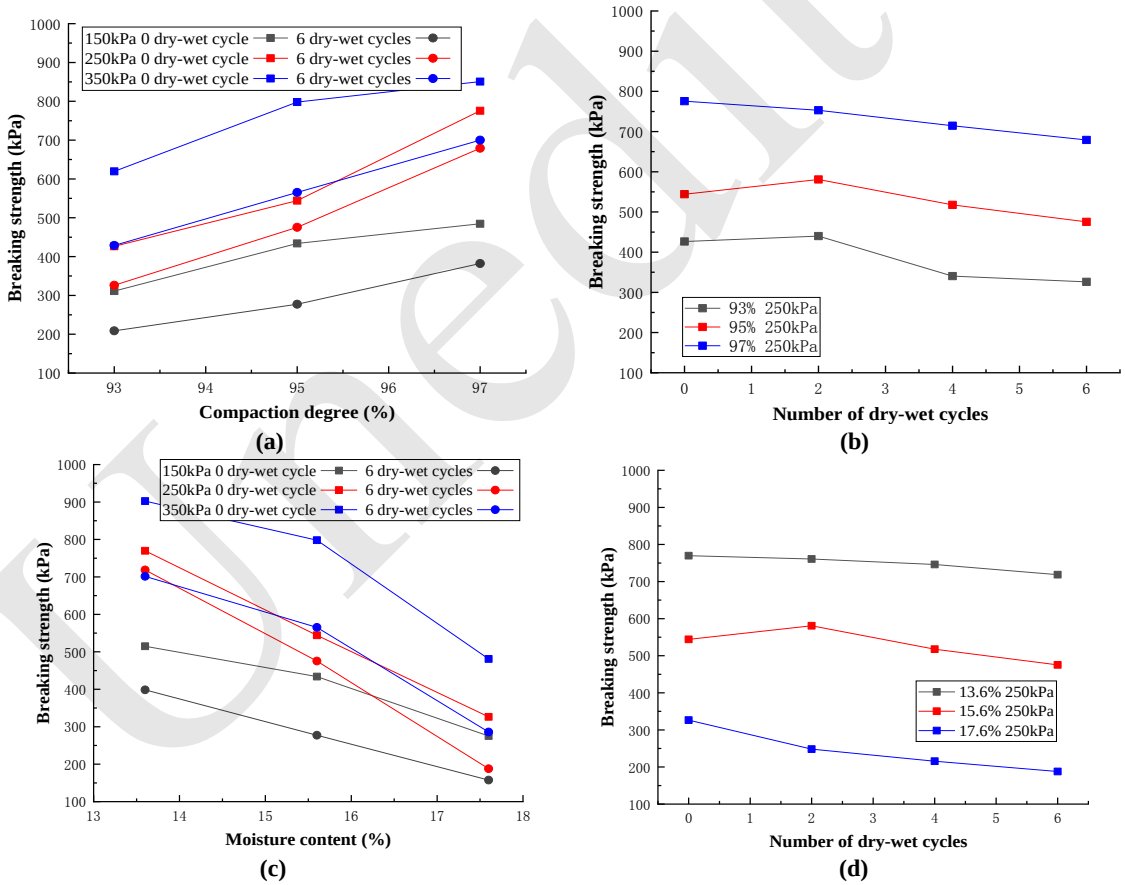

Fig. 8. Failure strength curves from triaxial testing of different soil samples. Effects of (a) compaction degree and confining pressure, (b) compaction degree and number of dry–wet cycles, (c) initial moisture content and confining pressure, and (d) initial moisture content and number of dry–wet cycles

Uncorrected

3.1.3 Shear strength parameters

The main indicators of soil shear strength, namely, the cohesion and internal friction angle (φ), were determined by combining the triaxial test data with Mohr's circle method. Fig. 9 shows that the cohesion and φ decreased with increasing dry–wet cycles and stabilized at different compaction degrees and initial moisture contents. The overall decrease in φ was negatively correlated with the compaction degree. The φ values of samples compacted at low pressures initially increased briefly but decreased in the long term, possibly because water drove the movement of internal soil particles during dry–wet cycling. The connections between particles changed from relatively ordered to disordered and then rearranged along the water transport channels This induced a slight increase in φ followed by a decrease. For example, at 93% compaction, the φ value increased by 2.9% to 17.1% after four dry–wet cycles, and then decreased by 6.5% after six dry–wet cycles. This trend was less likely to occur at a high compaction degree.

Fig. 9b shows that, at a less-than-optimal initial moisture content, the cohesion occasionally increased with increasing dry–wet cycles but exhibited an overall decrease. When initial moisture content was close to or greater than the optimal value, the cohesion decreased with increasing dry–wet cycles. This behavior may be due to the development of the soil toward the liquid-limit state at moisture contents greater than the optimal value, and the fact that dry–wet cycling increases the free water–occupied space between soil particles and thus reduces the cohesion. At different moisture contents, the overall φ value of the soil decreased. At a constant number of dry–wet cycles, φ increased steadily with increasing moisture content.

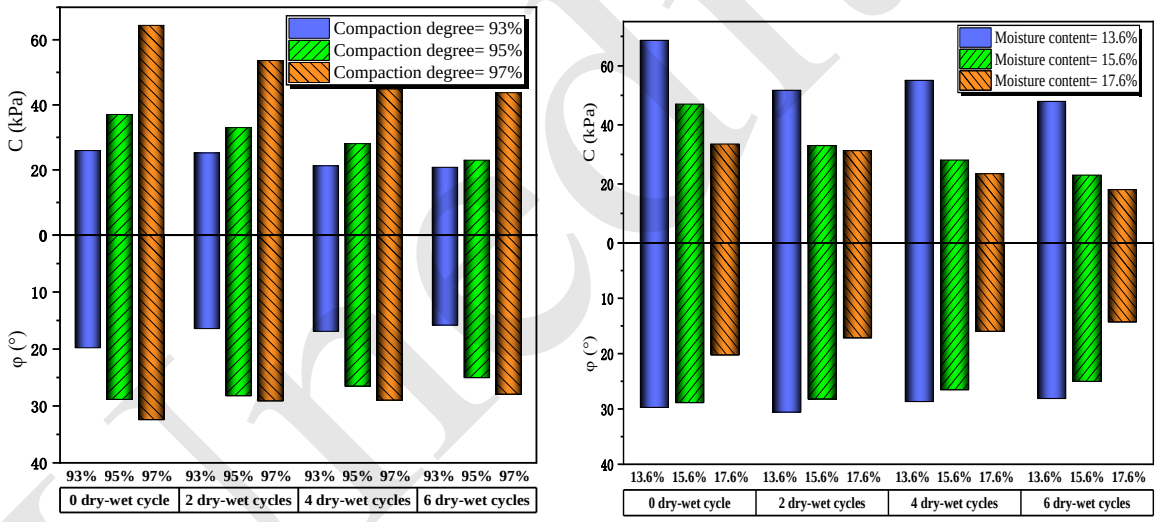

Fig. 9 Effects of (a) compaction degree and dry–wet cycling and (b) moisture content and dry–wet cycling on shear strength

3.1.4 Elastic modulus

The elastic modulus can be determined by fitting the tangent modulus to the elastic straight-line segment of the deviatoric stress–strain curve or by selecting the ratio of deviatoric stress to the strain increment at 1.5% strain. In this study, we used the latter method. Figs. 10a and 10b show that, at a constant confining pressure and initial moisture content, the elastic modulus increased with increasing compaction degree. The increase between 95% and 97% was greater than that between 93% and 95%. The elastic modulus decreased slightly as the number of dry–wet cycles increased.

Figs. 10c and 10d show that, at a constant compaction degree and confining pressure, the elastic modulus decreased as the initial moisture content increased. The decrease between 13.6% and 17.6% at a confining pressure of 350 kPa was lower than that under other conditions. This may be because the degree of decrease in the elastic modulus caused by a slight increase in moisture content is reduced with

increasing confining pressure. At a confining pressure of 150 kPa and zero dry–wet cycles, the elastic moduli at initial moisture contents of 13.6%, 15.6%, and 17.6% were 31.21 (−0%), 24.65 (−21%), and 15.33 (−38%) MPa, respectively. At six dry–wet cycles and initial moisture contents of 13.6%, 15.6%, and 17.6%, the elastic moduli were 30.57, 12.61, and 9.84 MPa, respectively. Compared to those observed at the same moisture content and zero dry–wet cycles, these values were lower by 2.06%, 48.84%, and 35.83%, respectively.

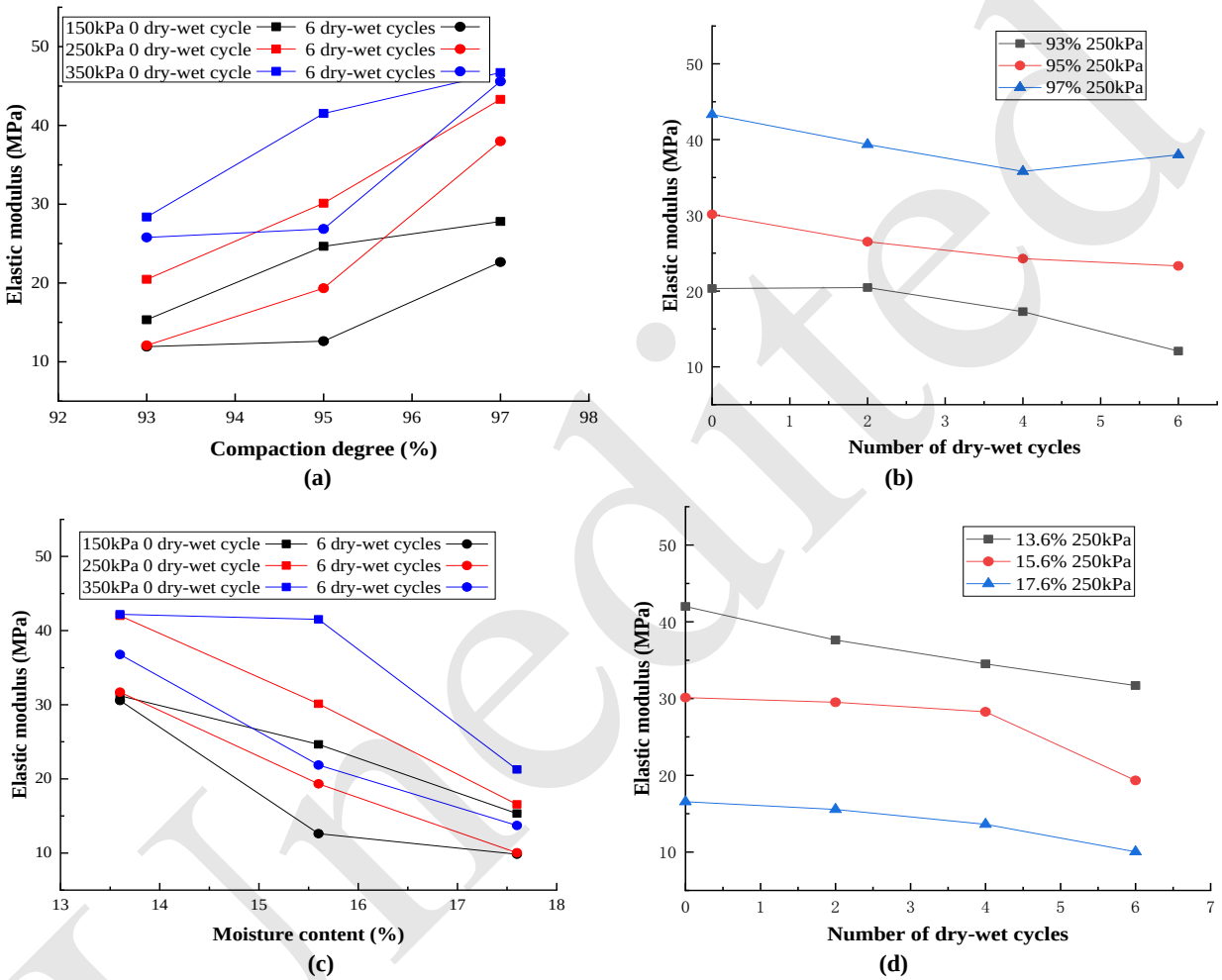

Fig. 10. Effects of (a) compaction degree and confining pressure, (b) compaction degree and dry–wet cycling, (c) initial moisture content and confining pressure, and (d) initial moisture content and dry–wet cycling on elastic modulus

3.2 Effects of dry–wet cycling on soil microstructure

Fig. 11 shows variable-magnification SEM images of the soil samples. Figs. 11a–11d indicate that, after zero to two dry–wet cycles at a constant initial moisture content and compaction degree, many fine particles were adhered to the sample surface in large-particle-size clusters or embedded in pores. With increasing dry–wet cycles, the number of fine particles decreased, while the pores and voids became larger and deeper, exposing the rounded boundaries of the larger particles. Figs. 11e–11g suggest that, at a constant compaction degree and zero dry–wet cycles, the sample with 13.6% initial moisture had more plate-like and angular coarse particles than the higher-moisture content samples. The boundary angles were clear and uneven, and cracks with larger angles were observed between the particles. This could be the reason for the larger φ values. As the initial moisture content was increased further, the angular boundaries of the coarse particles

Uncited

weakened, and some boundaries changed from angular to honeycomb-shaped, with smaller and more rounded cracks and pores, resulting in a more uniform shape.

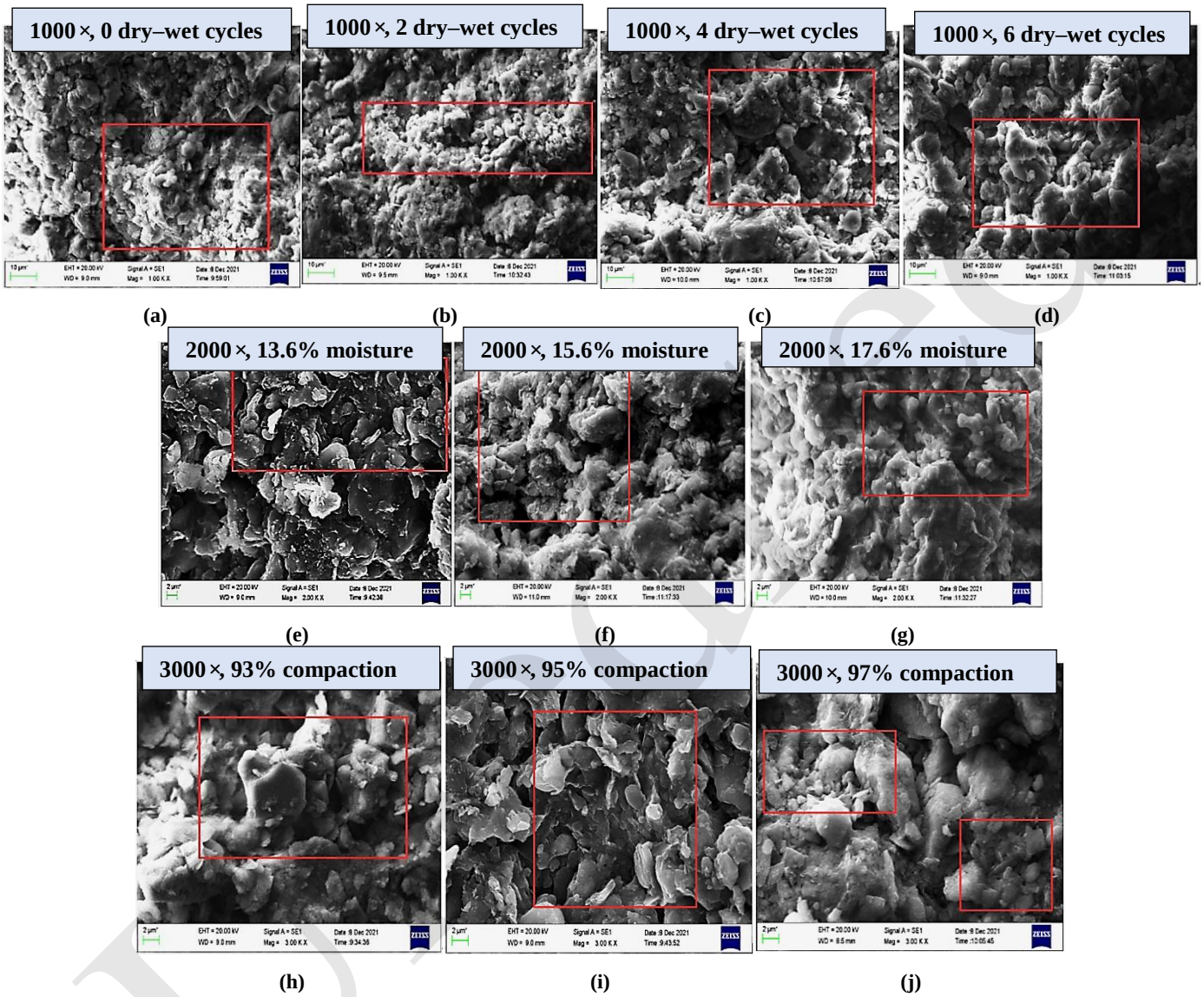

Fig. 11. Scanning electron microscopy images of different soil samples. Effects of (a)–(d) number of dry–wet cycles (zero, two, four, and six, respectively; 1000× magnification); (e)–(f) initial moisture content (13.6%, 15.6%, and 17.6%, respectively; 2000× magnification); and (h)–(j) compaction degree (93%, 95%, and 97%, respectively; 3000× magnification)

Figs. 11h–11j show that, at a constant initial moisture content and dry–wet cycle= 0, the pores and cracks observed in the samples with smaller compaction degrees were deeper, and larger particle size clusters and stepped skeleton connection structures were observed. As the compaction degree increased, the particle morphology changed from smooth to flat with more plate- and sheet-like particles and fewer but clearer cracks. When the compaction degree increased to 97%, the number of small particles attached to soil aggregates decreased, and these particles became more embedded in the cracks; that is, the number of pores and holes decreased. The undulation between the large skeleton particles was gentle, with no prominent stepped structure.

Figs. 12 and 13 show the results of SEM image processing using IPP.V6. The proportion of internal pores substantially increased after the first two cycles and then stabilized. At zero dry–wet cycles, the proportion of particles within each particle size range

was relatively balanced, with finer and fewer coarse particles. With increasing dry–wet cycles, the proportion of fine particles decreased, and that of coarse particles increased. The pore–particle ratio diagrams of samples with different initial moisture contents indicate that the lowest porosity and highest density were obtained at 15.6% initial moisture, which is related to the proximity of this initial moisture content to the optimal value. However, samples with 13.6% and 17.6% initial moisture had higher pore ratios. At a low initial moisture content, the particle sizes were concentrated at 5–10 μm, while the content of particles with other sizes was much lower, and the particle size distribution was relatively uneven. At medium and high initial moisture contents, fine particles were predominantly observed, while larger particles were less distributed and less abundant than that at a low initial moisture content. This may be related to the increased free water content inside large particles at high initial moisture contents, which promotes disintegration into smaller particles.

The pore–particle ratio decreased with increasing compaction degree, which improved the overall stress of the samples with high compaction degrees. At low compaction degrees, the overall content of large particles was relatively high, and the skeleton was relatively loose. At 95% compaction, the content of large particles decreased, the content of medium-sized (10–15 μm) particles decreased to zero, and the content of small (5–10 μm) particles increased substantially. This may be due to fragmentation of the loose large particles during compaction, which would have increased the content of small particles. With a further increase in compaction degree, the content of small particles decreased, and medium-sized particles reappeared, which resulted in a more uniform distribution of particles of each size.

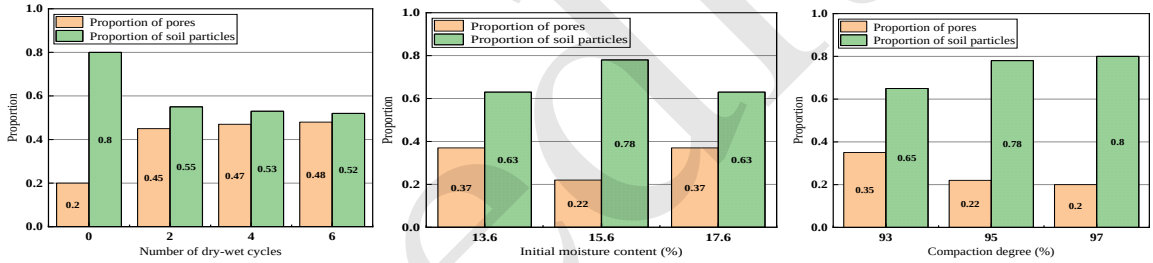

Fig. 12. Effects of (a) dry–wet cycling, (b) initial moisture content, and (c) compaction degree on the pore–particle ratio

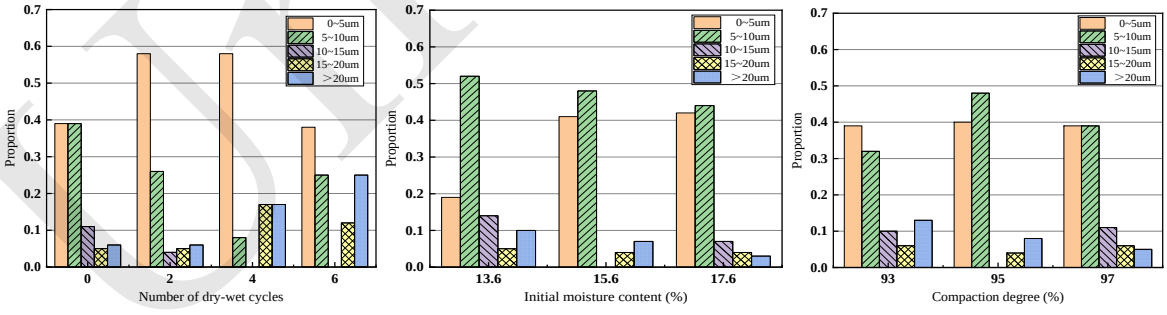

Fig. 13. Effects of (a) dry–wet cycling, (b) initial moisture content, and (c) compaction degree on the proportion of particles in different particle size ranges

3.3 Correlation between macroscopic and microscopic properties of soil and normalized expression of stress characteristics under dry–wet cycling

3.3.1 Correlation between macroscopic and microscopic properties of soil

Table 2 classifies the samples and summarizes the results of the triaxial shear tests and SEM imaging. When the initial moisture content and number of dry–wet cycles remained unchanged, increasing the compaction degree increased the peak value of the

stress–strain curve; that is, the mechanical performance was enhanced. With increasing compaction degree, the degree of embedding, particle size distribution balance, and large particle skeleton density improved to varying degrees, and the stress performance and index parameters, therefore, became more conducive for roadbed stability and resistance to dry–wet cycling-induced degradation. This will improve the roadbed performance under frequent rainfall conditions. With increasing moisture content, the angular boundaries of the soil particles gradually became blurred and turned more ellipsoidal/spherical. The angle between the particles was negatively correlated with the skeleton embedding degree and positively correlated with the stacking degree of the contact skeleton. The proportion of small and medium-sized particles also increased, and some large skeleton particles collapsed into small particles, thereby inducing mechanical property deterioration.

In summary, when selecting fine breccia soil for foundation treatment, soil with a higher compaction degree and slightly lower initial moisture content should be selected for use as fill. Frequent rainfall in the local area is more conducive to durability and stability, and greater cohesion and φ favor resistance to the loss of soil particles to hidden soil caves and karst channels under seepage.

Table 2 Summary of soil properties and structural characteristics under different working conditions

Variable	Value	Microscopic features	Stress peak	Failure strength	Cohesion	φ	Elastic modulus
Compaction degree	93%	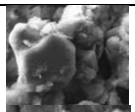	small	small	small	small	small
	95%		medium	medium	medium	medium	medium
	97%		large	large	large	large	large
Moisture content	13.6%		large	large	large	large	large
	15.6%	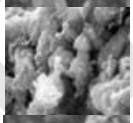	medium	medium	medium	medium	medium
	17.6%	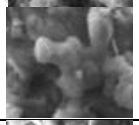	small	small	small	small	small
Dry–wet cycles	0		large	large	large	large	large
	2		medium	medium	medium	medium	medium
	4	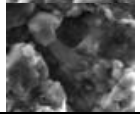	small	small	small	small	small

3.3.2 Normalization characteristics of soil under

Uncited

dry–wet cycling

Different methods and factors have been proposed for normalizing the mechanical properties of soil. Among them, Konder's normalization method (Duncan and Chang, 1970), which is based on hyperbolic equations and normalization factors, fits the results of static triaxial tests and features normalization conditions that are relatively easy to meet. The related expressions are as follows:

$$\sigma_1 - \sigma_3 = \varepsilon_1/(a_i\varepsilon_1 + b_i), \quad (1)$$

$$\varepsilon_1/(\sigma_1 - \sigma_3) = a_i\varepsilon_1 + b_i, \quad (2)$$

where a_i is the reciprocal of the ultimate deviator stress $(\sigma_1 - \sigma_3)_u$ under a certain confining pressure, and b_i is the reciprocal of the initial tangent modulus E_i. Equation (2) shows that the linear relationship between the ratio of axial strain to the deviator stress and axial strain has a slope of a_i and longitudinal intercept of b_i. At different confining pressures (σ_3), the a_i and b_i normalization results for the same soil sample differ. To obtain the stress–strain normalization relationship at different confining pressures, one can multiply both sides of Equation (2) by a normalization factor A_i:

$$A_i\varepsilon_1/(\sigma_1 - \sigma_3) = A_ia_i\varepsilon_1 + A_ib_i. \quad (3)$$

Further,

$$M = A_ia_i,\ N = A_ib_i. \quad (4)$$

Here, M and N are constants, indicating that the normalization condition is essentially a positive proportional relationship between the normalization factor A_i, ultimate deviator stress $(\sigma_1 - \sigma_3)_u$, and initial tangent modulus E_i. The commonly used normalization factors and their normalization conditions are listed in Table 3.

Table 3 Statistical analysis parameters of fitting results

Normalization factor	σ_3	σ_m	$(\sigma_1 - \sigma_3)_u$	$(\sigma_3)^n$
Normalization conditions	$(\sigma_1 - \sigma_3)_u$, $E_i \propto \sigma_3$	$(\sigma_1 - \sigma_3)_u$, $E_i \propto \sigma_m$	$(\sigma_1 - \sigma_3)_u$ $\propto E_i$	$(\sigma_1 - \sigma_3)_u$, $E_i \propto (\sigma_3)^n$

Table 3 suggests that relatively few limiting conditions exist when the ultimate deviator stress is used as a normalization factor. Therefore, this study used the ultimate deviator stress as a normalization factor to fit and analyze the stress–strain curves of a 1.5-m-buried soil sample with a compaction degree of 95% and initial moisture content of 15.6% at confining pressures of 150, 250, and 350 kPa. Equation (2) was applied to fit the stress–strain curves in Figs. 7a–7c. Data points near the starting point of the curve were removed during the loading process. The results are shown in Fig. 14, and the fitting parameters are summarized in Table 4.

Table 4 Relationship-fitting parameters of $\varepsilon_1/(\sigma_1 - \sigma_3)$ and ε_1

σ_3 (kPa)	Cyc. no.	a_i $\times 10^3$	b_i $\times 10^5$	$(\sigma_1 - \sigma_3)_u$ (kPa)	E_i (MPa)	R^2
150	0	2.25	0.88	444.44	113.97	0.9998
150	2	2.62	1.49	381.68	67.33	0.9998
150	4	3.01	1.77	332.23	56.56	0.9996
150	6	3.44	2.67	290.70	37.46	0.9991
250	0	1.76	0.72	568.18	139.20	0.9991
250	2	1.58	1.89	632.91	52.85	0.9849
250	4	1.89	0.99	529.10	100.56	0.9995
250	6	1.93	2.72	518.13	36.70	0.9934
350	0	1.22	0.64	819.67	155.46	0.9993
350	2	1.31	0.91	763.36	109.33	0.9999
350	4	1.55	0.76	645.16	131.71	0.9975

When $(\sigma_1 - \sigma_3)_u$ is zero, E_i is also zero. Linear fitting was performed on the data of $(\sigma_1 - \sigma_3)_u$ and E_i at different confining pressures and dry–wet cycle numbers, with the initial value of the fitting curve being (0, 0). The obtained fit is shown in Fig. 15, and the fitting expression is given by Equation (5). The coefficient of determination (R^2) equaled 0.88. Linear fitting was performed for the relationship between the ultimate deviator stress and the confining pressure at zero dry–wet cycles. The results are shown in Fig. 16 and Equation (6) ($R^2 = 0.97$).

$$(\sigma_1 - \sigma_3)_u = 0.00552E_i, \quad (5)$$

$$(\sigma_1 - \sigma_3)_{u0} = 1.88\sigma_3 + 141.73. \quad (6)$$

where $(\sigma_1 - \sigma_3)_{ui}$ and E_i represent the ultimate deviator stress and initial tangent modulus, respectively, after the i^{th} dry–wet cycle. The residual strength ratio after the i^{th} dry–wet cycle is defined as $Q_i = (\sigma_1 - \sigma_3)_{ui}/(\sigma_1 - \sigma_3)_{u0}$ and reflects the ability of the soil to resist degradation by dry–wet cycling. The larger the value of Qi, the better the soil can resist the degra-

Unedited

dation effect of dry–wet cycling and the better suited it is to use in areas with high rainfall. When $(\sigma_1-\sigma_3)_{ui}$ is used as the fitting normalization factor, the fitting expression becomes

$$\varepsilon_1(\sigma_1-\sigma_3)_{ui}/(\sigma_1-\sigma_3)=(\sigma_1-\sigma_3)_{ui}a_i\varepsilon_1+(\sigma_1-\sigma_3)_{ui}b_i. \quad (7)$$

Based on the residual strength ratio and Equations (5) and (6), the relationship between the stress characteristics of fine breccia soil in karst areas under dry–wet cycling can be expressed as follows:

$$(\sigma_1-\sigma_3)=Q_i\varepsilon_1(1.88\sigma_3+141.73)/(0.00552+\varepsilon_1). \quad (8)$$

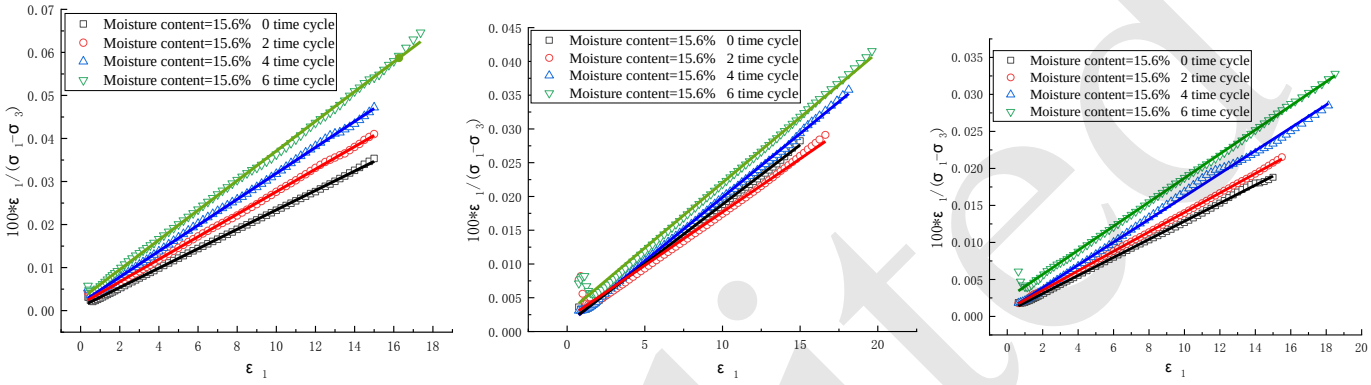

(a) **(b)** **(c)**

Fig. 14. Relationship between $\varepsilon_1/(\sigma_1-\sigma_3)$ and ε_1 at different dry–wet cycle and confining pressures = (a) 150, (b) 250, and (c) 350 kPa

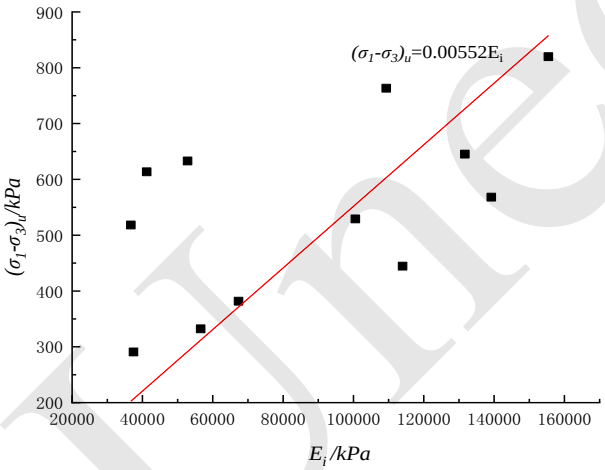

Fig. 15 Relationship between $(\sigma_1-\sigma_3)_u$ and E_i.

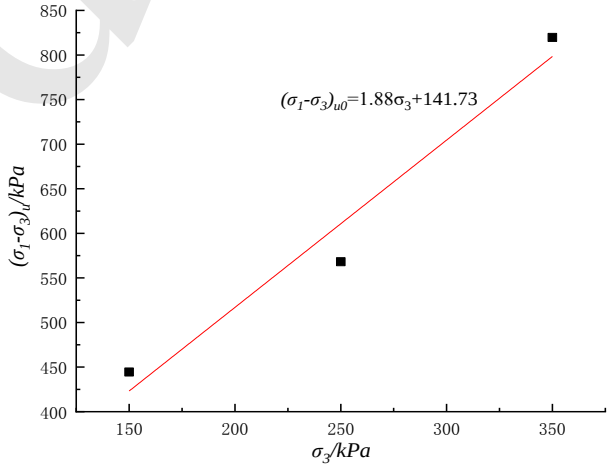

Fig. 16 Relationship between σ_3 and $(\sigma_1-\sigma_3)_u$

5 Conclusions

Triaxial shear tests and SEM were employed to study the mechanical properties and microscopic characteristics of fine breccia soil from karst areas. This testing facilitated an in-depth analysis and comparison of the physical and mechanical properties, microstructures, micro-to-macro correlations, and damage models of *in situ* roadbed fill in karst areas under prolonged dry–wet cycling. The follow-

Uncited

ing conclusions can be drawn from the results of the study.

1. The deformation behavior of fine breccia soil in karst terrains exhibits a stress-hardening trend. The peak stress in the soil is directly correlated to the compaction degree and confining pressure and inversely correlated to the moisture content and number of dry–wet cycles. Soil that underwent high-pressure compaction and maintained an initial moisture content close to the optimal value exhibited enhanced resistance to degradation due to dry–wet cycling.

2. For fine breccia soil in karst regions that underwent high-pressure compaction, the failure strength, shear strength, and elastic modulus remained relatively unaffected by dry–wet cycling. However, the values of these properties decreased at high water contents and particularly at high confining pressures.

3. An increased degree of compaction improved the soil's particle size distribution and skeleton density, enhancing its mechanical properties and performance indicators. This should make the roadbed more resilient against the erosive impact of dry–wet cycling, ensuring better stability, especially under frequent rainfall conditions. Conversely, a rise in moisture content blurred the angular demarcations of soil particles. The increased angularity between particles led to a decline in the structural integrity of the embedded skeleton, causing larger skeletal particles to disintegrate into smaller ones, adversely impacting the soil's mechanical properties and roadbed stability.

4. A normalized stress–strain model was formulated to leverage the results from multifaceted condition triaxial and microscanning tests on Jiangxi fine breccia soil. This model incorporated the effects of confining pressures and dry–wet cycling by integrating the residual strength ratio associated with dry–wet cycling. The study further recommends that techniques promoting higher compaction degrees and slightly sub-optimal moisture contents be preferred for optimal stability when utilizing fine breccia soil from karst areas as roadbed fill.

Acknowledgments

This work was financially supported by grants from the National Natural Science Foundation of China (No. 52108377), the National Natural Science Foundation of China-Key Project (No. 51938008), and the Foundation for Basic and Applied Basic Research of Guangdong Province (No. 2023A1515010060).

Author contributions

Xin Li: Validation, Investigation, Conceptualization, Methodology, Formal analysis, Writing – original draft. **Hanqing Chen:** Investigation, Writing – review and editing. **Dong Su:** Funding acquisition, Supervision. **Xiangsheng Chen:** Funding acquisition, Supervision. **Xiang Shen:** Writing – review and editing.

Conflict of interest

The authors declare no known economic or personal competitive interests or relationships affecting the publication of this article.

Data availability

Data will be made available on request.

References

Celauro C, Corriere F, Guerrieri M, *et al.*, 2017. Environmental analysis of different construction techniques and maintenance activities for a typical local road. *Journal of Cleaner Production*, 142(4):3482-3489. https://doi.org/10.1016/j.jclepro.2016.10.119

Chao Z, Shi D, Fowmes G, 2023. Mechanical behaviour of soil under drying–wetting cycles and vertical confining pressures. *Environmental Geotechnics*, Ahead of print. https://doi.org/10.1680/jenge.22.00048

Chen R, Cai G, Dong X, *et al.*, 2019. Mechanical properties and micro-mechanism of loess roadbed filling using by-product red mud as a partial alternative. *Construction and Building Materials*, 216:188-201. https://doi.org/10.1016/j.conbuildmat.2019.04.254

Deng Y, Wang S, Bai X, *et al.*, 2020. Spatiotemporal dynamics of soil moisture in the karst areas of China based on reanalysis and observations data. *Journal of Hydrology*, 585:124744. https://doi.org/10.1016/j.jhydrol.2020.124744

Drobinina E, Kovaleva T, Koriakina A, 2020. The local variation of the overlying soils geotechnical properties in the karst susceptibility assessment. *Carbonates and Evaporites*, 35:79. https://doi.org/10.1007/s13146-020-00615-3

Duncan JM, Chang C-Y, 1970. Nonlinear analysis of stress and strain in soils. *Journal of the Soil Mechanics and Foundation*, 96(5):1629-1653. https://doi.org/10.1061/JSFEAQ.0001458

Fang JJ, Yang XL, Feng YX, *et al.*, 2021. True triaxial experimental study on mechanical properties of expansive soils after drying and wetting cycles. *Chinese Journal of Rock Mechanics and Engineering*, 40(5):1043-1055.

Feng S, Lei H, 2022. A settlement prediction model considering tidal loading and traffic loading of soft soil subgrade. *Computers and Geotechnics*, 144:104639. https://doi.org/10.1016/j.compgeo.2022.104639

Uncorrected

Geng D, Meng C, Wang J, *et al.*, 2022. Coupling influence of rainfall infiltration and traffic load on silt roadbed. *Journal of Chongqing Jiaotong University (Natural Sciences)*, 6:98-104. (in Chinese)
https://doi.org/10.3969/j.issn.1674-0696.2022.06.15

Goh SG, Rahardjo H, Leong EC, 2014. Shear strength of unsaturated soils under multiple drying-wetting cycles. *Journal of Geotechnical and Geoenvironmental Engineering*, 140(2):06013001.
https://doi.org/10.1061/(ASCE)GT.1943-5606.0001032

Han J, Zhao G-T, Sheng X-Z, *et al.*, 2016. Study on the subgrade deformation under high-speed train loading and water–soil interaction. *Acta Mechanica Sinica*, 32:233-243.
https://doi.org/10.1007/s10409-015-0522-6

Huang G, Zheng M, 2021. Effect of dry-wet cycling on the residual strength characteristics of coal measure soil. *KSCE Journal of Civil Engineering*, 25:4184-4195.
https://doi.org/10.1007/s12205-021-2147-6

Hu W, Cheng W-C, Wen S, *et al.*, 2021. Effects of chemical contamination on microscale structural characteristics of intact loess and resultant macroscale mechanical properties. *Catena*, 203:105361.
https://doi.org/10.1016/j.catena.2021.105361

Ibrahim OR, Al Maqbali LA, Al Shaqsi MS, 2022. Comparison between sediment material and natural subgrade material for road construction. *Key Engineering Materials*, 913:215-226.
https://doi.org/10.4028/p-yj1y51

Khalid RA, Ahmad N, Arshid MU, *et al.*, 2022. Performance evaluation of weak subgrade soil under increased surcharge weight. *Construction and Building Materials*, 318:126131.
https://doi.org/10.1016/j.conbuildmat.2021.126131

Kong X, Wang G, Liang Y, *et al.*, 2022. The engineering properties and microscopic characteristics of high-liquid-limit soil improved with lignin. *Coatings*, 12(2):268.
https://doi.org/10.3390/coatings12020268

Li S, He Z, Zhu P, *et al.*, 2022. Experimental study on the triaxial compression properties of coarse-grained filling soil under drying–wetting cycles. *Geofluids*, 2022:1452916.
https://doi.org/10.1155/2022/1452916

Li W, Zeng S, Zhao J, *et al.*, 2017. Damage characteristics of Changsha ring expressway silty clay during dry-wet cycle. *Journal of Central South University of Technology*, 48(5):1360-1366.

Li Y, Liu J, 2020. Mechanical behavior and microstructure of crude-oil-polluted structural loess in Nanjing City, China. *Journal of Porous Media*, 23(2):163-176.
https://doi.org/0.1615/JPorMedia.2019027086

Li Z, Guan C, Han M, *et al.*, 2022. Estimation of settlement in loess-filled subgrade with consideration of lateral deformation. *Arabian Journal for Science and Engineering*, 47:4713-4729.
https://doi.org/10.1007/s13369-021-06247-6

Lin B, Cerato AB, 2015. Shear strength of shale weathered expansive soils along swell-shrink paths: Analysis based on microscopic properties. *Environmental Earth Sciences*, 74:6887-6899.
https://doi.org/10.1007/s12665-015-4691-1

Lu Z, Fang R, Chen L, *et al.*, 2020. Long-term deformation of highway subgrade under coupling effect of traffic load and drying–wetting cycles. *International Journal of Geomechanics*, 20(2):04019168.
https://doi.org/10.1061/(ASCE)GM.1943-5622.0001568

Luo Y, Meng J, Wang D, *et al.*, 2022. Experimental study on mechanical properties and microstructure of metakaolin based geopolymer stabilized silty clay. *Construction and Building Materials*, 316:125662.
https://doi.org/10.1016/j.conbuildmat.2021.125662

Liu WH, 2015. Effect of drying/wetting on the mechanical behaviors of unsaturated soils and study on the constitutive relationship of unsaturated soils. PhD Thesis, Dalian University of Technology, Dalian, China.(in Chinese)

Mingjing J, 2019. New paradigm for modern soil mechanics: Geomechanics from micro to macro. *Chinese Journal of Geotechnical Engineering*, 41(2):195-254.
https://doi.org/10.11779/CJGE201902001

Mu K, Kong LW, Zhang XW, *et al.*, 2016. Experimental investigation on engineering behaviors of red clay under effect of wetting-drying cycles. *Rock and Soil Mechanics*, 37(8):2247-2253. (in Chinese)
https://doi.org/10.16285/j.rsm.2016.08.016

Que Y, Zhang H, Zhu T, *et al.*, 2022. Amending foamed lightweight soil with tailings sand for embankment applications: Physical properties, durability, and microstructure. *Construction and Building Materials*, 350:128912.
https://doi.org/10.1016/j.conbuildmat.2022.128912

Raja K, Vishnuvardhan K, Venkatachalam S, *et al.*, 2022. Strength and settlement of subgrade soil in southern part of Kangeyam block. *Materials Today: Proceedings*, 65(2):1930-1938.
https://doi.org/10.1016/j.matpr.2022.05.173

Smirnova MA, Gennadiev AN, 2011. Soils of karst sinkholes in the southeast of the Belomorsk-Kuloi Plateau. *Eurasian Soil Science*, 44:117-125.
https://doi.org/10.1134/S106422931102013X

Song BH, Han C, Chen JH, *et al.*, 2015. Subgrade design and construction technology for saline soil area. *Applied Mechanics and Materials*, 744-746:641-646.
https://doi.org/10.4028/www.scientific.net/AMM.744-746.641

Sun Y, Meng S, Wang M, *et al.*, 2021. Deterioration effect of freeze-thaw on mechanical properties of roadbed clay under unfavorable conditions. *Bulletin of Engineering Geology and the Environment*, 80:4773-4790.
https://doi.org/10.1007/s10064-021-02203-8

Wang LC, 2014. Experimental study on dynamic characteristics of subgrade soil under cyclic load in karst area. *Mining and Metallurgical Engineering*, 34:16-18.

Wang L, Cheng W-C, Xue Z-F, 2022. Investigating microscale

structural characteristics and resultant macroscale mechanical properties of loess exposed to alkaline and saline environments. *Bulletin of Engineering Geology and the Environment*, 81:146. https://doi.org/10.1007/s10064-022-02640-z

Wen T, Shao L, Guo X, 2021. Effect of hysteresis on hydraulic properties of soils under multiple drying and wetting cycles. *European Journal of Environmental and Civil Engineering*, 25(10):1750-1762. https://doi.org/10.1080/19648189.2019.1600037

Xiao J, Liu J, Hou Y, *et al.*, 2007. Experimental study on mechanical properties of rock-salt for subgrade fill material. *Journal of Engineering Geology*, 15(1):119-123.

Xin L, Mingzhou B, Zijun W, *et al.*, 2021. Dynamic response and stability analysis of high-speed railway subgrade in karst areas. *IEEE Access*, 9:129188-129206. https://doi.org/10.1109/ACCESS.2021.3113706

Xu J, Wang Y, Yan C, *et al.*, 2019. Lifecycle health monitoring and assessment system of soft soil subgrade for expressways in China. *Journal of Cleaner Production*, 235:138-145. https://doi.org/10.1016/j.jclepro.2019.06.256

Yong H, Zirui L, Shaoshuai T, *et al.*, 2020. Effect of average particle size on shear properties of sand and its mesomechanical analysis. *Journal of Jilin University (Earth Science Edition)*, 50(6):1814-1822. (in Chinese) https://doi.org/10.13278/j.cnki.jjuese.20190081

Yuan K-z, Ni W-k, Lü X-f, *et al.*, 2021. Permeability characteristics and structural evolution of compacted loess under different dry densities and wetting-drying cycles. *PLoS One*, 16(6):e0253508. https://doi.org/10.1371/journal.pone.0253508

Yu J, Chen D, Wang H, *et al.*, 2019. Analysis of the shear strength of granite residual soil and slope stability under wetting-drying cycles. *Journal of Xiamen University (Natural Science)*, 58(4):614-620.

Zeng L, Yu H-C, Gao Q-F, *et al.*, 2022. Evolution of tensile properties of compacted red clay under wet and dry cycles. *KSCE Journal of Civil Engineering*, 26:606-618. https://doi.org/10.1007/s12205-021-0527-6

Zhou LJ, 2012. Subgrade stability analysis with rainfall infiltration. *Applied Mechanics and Materials*, 204-208:284-288. https://doi.org/10.4028/www.scientific.net/AMM.204-208.284

中文概要

题　目：干湿循环对岩溶地区细角砾土力学性质和微观特征的影响

作　者：李鑫[1,2,3]，陈汉青[1,2,3]，苏栋[1,2,3]，陈湘生[1,2,3]，沈翔[1,2,3]

机　构：[1]深圳大学，土木与交通工程学院，未来地下城市研究院，中国深圳，518060；[2]深圳大学，滨海城市韧性基础设施教育部重点实验室，中国深圳，518060；[3]深圳大学，深圳市地铁地下车站绿色高效智能建造重点实验室，中国深圳，518060

目　的：在干-湿循环的过程中岩溶区细角砾土的微观性能与宏观力学特性会发生变化导致路基性能的改变。本文旨在探讨不同干-湿循环次数后，土体的微观特征（颗粒组成、孔隙结构等）及宏观力学性能（应力-应变关系、破坏强度等）在不同初始含水率、压实度等条件下的变化趋势，研究干-湿循环作用下土体力学特性与微观特征间的关联，提出岩溶区细角砾土在路基中的使用建议。

创新点：1.基于 Konder 应力-应变归一化方程，引入干-湿循环强度残余比概念，推导出不同环境变量下细角砾土应力-应变关系表达式；2. 通过微观特征数据提取与宏观力学试验，建立了干-湿循环作用下细角砾土力学特性与微观特征间的相互关联。

方　法：1. 通过试验分析，得到不同压实度、初始含水率和围压下，干-湿循环对岩溶区细角砾土的宏观力学性能的影响规律；2. 通过理论推导，构建了引入干-湿循环强度残余比概念的细角砾土应力-应变关系归一化表达式；3. 通过电镜扫描试验和图像数据提取技术，得到了不同干-湿循环次数下，不同条件下岩溶区细角砾土的微观结构及相关数据，并于宏观力学性质相互关联。

结　论：1. 岩溶区细角砾土受力变形呈应力硬化型，高压实度和接近最佳含水率的土壤更能抵抗干湿循环的劣化效应；2. 高含水率使土颗粒的棱角边界模糊，颗粒间大夹角的嵌挤骨架减少，部分大骨架颗粒崩解为小颗粒，导致其力学性质减弱；3. 以岩溶区细角砾土为路基填料时，建议选用大压实度和略小于最佳含水率的方法进行填筑。

关键词：岩溶地质；微-宏观特性；路基性能；干-湿循环